Silvanus Thompson Memorial Lecture
Molecular imaging using hyperpolarized [13]C

[1]K GOLMAN, PhD, [1]L E OLSSON, PhD, [1]O AXELSSON, PhD, [2]S MÅNSSON, PhD, [1]M KARLSSON, PhD and [1]J S PETERSSON, PhD

[1]*Amersham Health R&D AB, Medeon, SE-205 12 Malmö and* [2]*Department of Experimental Research, Malmö University Hospital, SE-205 02 Malmö, Sweden*

Abstract. MRI provides unsurpassed soft tissue contrast, but the inherent low sensitivity of this modality has limited the clinical use to imaging of water protons. With hyperpolarization techniques, the signal from a given number of nuclear spins can be raised more than 100 000 times. The strong signal enhancement enables imaging of nuclei other than protons, *e.g.* [13]C and ^{15}N, and their molecular distribution *in vivo* can be visualized in a clinically relevant time window. This article reviews different hyperpolarization techniques and some of the many application areas. As an example, experiments are presented where hyperpolarized ^{13}C nuclei have been injected into rabbits, followed by rapid ^{13}C MRI with high spatial resolution (scan time <1 s and 1.0 mm in-plane resolution). The high degree of polarization thus enabled mapping of the molecular distribution within various organs, a few seconds after injection. The hyperpolarized ^{13}C MRI technique allows a selective identification of the molecules that give rise to the MR signal, offering direct molecular imaging.

Introduction

Thermal equilibrium polarization and hyperpolarization

The underlying principle of MRI is based on the interaction of atomic nuclei with an external magnetic field. A fundamental property of the atomic nucleus is the nuclear spin, described by the spin quantum number I. Many atomic nuclei have a non-zero spin quantum number and can be studied with nuclear magnetic resonance (NMR), *e.g.* [1]H, [3]He, ^{13}C, ^{15}N and [129]Xe. However, the clinical use of MRI has to date been restricted to ^{1}H, for reasons of sensitivity. Not only does ^{1}H have a higher sensitivity than any other nucleus in endogenous substances; it is also abundant in a very high concentration (about 80 M) in biological tissues.

Nuclei with spin quantum number $I = \frac{1}{2}$ (such as ^{1}H, [3]He and ^{13}C) can orient themselves in two possible directions: parallel ("spin up") or anti-parallel ("spin down") to the external field. The net magnetization per unit volume, and thus the available NMR signal, is proportional to the population difference between the two states. Denoting the number of spins in the "up" and "down" directions N^+ and N^-, respectively, the polarization P is by definition given as:

$$P = \frac{N^+ - N^-}{N^+ + N^-} \tag{1}$$

If the two populations are equal, their magnetic moments cancel, resulting in zero macroscopic magnetization, and thus no NMR signal. However, under thermal equilibrium conditions, slightly higher energy is associated with the "down" direction, and N^- will thus be slightly smaller than N^+ (see Figure 1). For a nucleus with spin quantum number $I = \frac{1}{2}$, the polarization P is given by:

$$P = \tanh\left(\frac{\gamma \hbar B_0}{2k_B T}\right) \tag{2}$$

where tanh refers to the hyperbolic tangens, B_0 is the magnetic field strength, γ the gyromagnetic ratio for the nucleus, T the temperature, k_B the Boltzmann constant and h the Planck constant. The thermal equilibrium polarization is very low: even at a magnetic field of 1.5 T it is only 5×10^{-6} for ^{1}H, and 1×10^{-6} for [13]C (at body temperature). In other words, only about one of a million nuclei contribute to the measured NMR signal in a standard clinical MRI scanner.

The polarization, and thereby the strength of the NMR signal, increases proportionally with the magnetic field [1], which has been the motivation for developing higher field MRI systems. Accordingly, 3 T instruments have been introduced for clinical whole body imaging [2]. Higher fields are technically achievable, but practical problems such as costs, radiofrequency penetration depths, and tissue contrast, increase dramatically with increasing field.

A conceptually different method to increase the polarization is to create an artificial, non-equilibrium distribution of the nuclei: the "hyperpolarized" state, where the population difference $N^+ - N^-$ is increased by several orders of magnitudes compared with the thermal equilibrium (Figure 1). The hyperpolarized state can be created *in vivo* by means of dynamic nuclear polarization (DNP) techniques, such as the Overhauser effect [3], in combination with a suitable contrast agent [4]. Alternatively, the hyperpolarized state of an imaging agent can be created by an external device, followed by rapid administration of the agent to the subject to be imaged. Examples of the latter approach include hyperpolarization of the noble gases [129]Xe [5] and [3]He [6] using optical pumping, and hyperpolarization of a wide range of organic molecules containing ^{13}C, by either parahydrogen-induced hyperpolarization [7] or DNP hyperpolarization [8].

Imaging of hyperpolarized agents

The concentration of a hyperpolarized imaging agent may be 0.5 M in the injection syringe and decrease to 1–20 mM *in vivo*, due to dilution in the vascular system. This is far below the typical ^{1}H concentration of 80 M, but since the hyperpolarization can enhance the signal up to
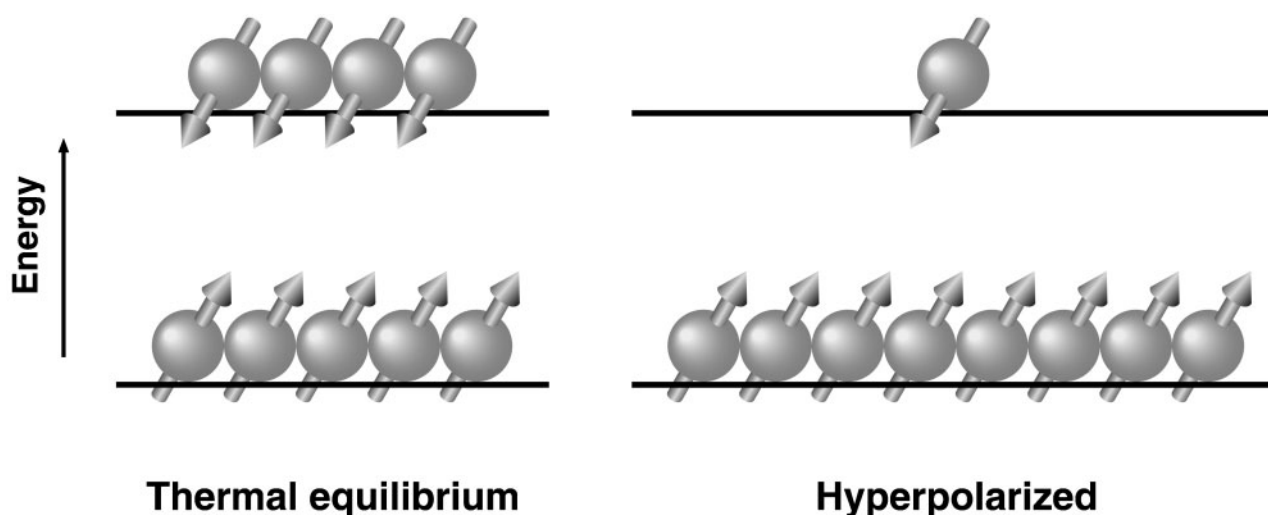
Figure 1. Pictorial description of the orientation of the nuclei at thermal equilibrium and in the hyperpolarized state. In the figure, the magnetic field (B_0) is directed vertically upwards.

10^6 times, MRI can be extended to nuclei other than ^1H, thereby permitting the visualization of changes in the molecular structure in a reasonable time frame, *e.g.* caused by metabolic processes, which were previously inaccessible.

The ability of conventional ^1H MRI to differentiate between various soft tissues and detect pathology is based mainly on the inherently different relaxation times (T_1, T_2 and T_2*) of different tissues. Even so, the achievable dynamic range is below 10 [9]. With the administration of contrast agents containing paramagnetic atoms (*e.g.* Gd^{3+}, Mn^{2+}), the relaxation rates ($1/T_1$, $1/T_2$) will increase proportionally with the concentration of the agent. Depending on the imaging sequence used, the reduced relaxation time can result in either an increased or a decreased signal where the agent accumulates, thereby increasing the image contrast [10]. The mechanism is fundamentally different for hyperpolarized agents: the hyperpolarized nuclei generate the signal themselves rather than moderating the signal from adjacent protons. Consequently, hyperpolarized MRI has the advantage of completely lacking background signal, either because the nuclei are not naturally present in the body (noble gases) or because the natural abundance signal is negligible (^{13}C). In this respect, hyperpolarized MRI behaves similarly to the modalities positron emission tomography (PET) and single photon emission computed tomography (SPECT), where the scanner detects the radiation from an injected contrast agent containing gamma-emitting nuclei, and where the signal strength is directly proportional to the concentration.

Hyperpolarization techniques

For practical purposes, four different methods exist to create a hyperpolarized state:

The ''brute force'' approach

From Equation (2), it follows that the thermal equilibrium polarization increases with increasing magnetic field strength and decreasing temperature. A straightforward, ''brute force'' approach to increase the polarization in a sample consists of subjecting it to a very strong magnetic field at a temperature close to absolute zero. The polarization, which is in the parts per million (ppm) range at 1.5 T and body temperature, can, for example, be increased by a factor of 1000 by cooling down the sample to liquid helium temperature (4 K) at a field strength of 20 T. If the sample is brought to 1.5 T and 310 K rapidly (*i.e.* without losses of polarization), it is thus hyperpolarized at body temperature. To obtain polarization levels where the hyperpolarized signal exceeds the ^1H signal of conventional MRI, the ''brute force'' method would require impractically low temperatures (in the mK range). Large-scale production of hyperpolarized noble gases (^3He and ^{129}Xe) has been proposed using this approach [11], but due to the great technical challenges and costs associated with these extremely low temperatures, the method has not yet been used for *in vivo* applications.

Dynamic nuclear polarization (DNP)

As seen in the previous section, low temperature and high magnetic field increases the polarization. Under moderate conditions, *e.g.* 1 K and 3 T, the nuclear polarization is still insufficiently low for ^{13}C MRI (polarization <0.1%), but electrons are highly polarized (>90%) due to the much larger gyromagnetic ratio of the electron (c.f. Equation (2)). Using the DNP technique, the high polarization of the electron spins can be transferred to coupled nuclear spins [12]. In the method described by Ardenkjaer-Larsen et al [8], the material containing the nuclei to be hyperpolarized is doped with a single-electron substance and exposed to a magnetic field of ~3 T and a temperature of ~1 K (Figure 2). Microwave irradiation near the electron resonance frequency transfers the polarization from the unpaired electrons to the ^{13}C nuclei, whereby the nuclear polarization in the solid material can be increased to 20–40%. By rapid melting and dissolving, the solid can be transformed into an injectable liquid, with small to negligible polarization losses.

Parahydrogen-induced polarization

In the parahydrogen-induced polarization (PHIP) method, nuclear polarization is increased via a chemical

Solid material doped with unpaired electrons

P_e= 94% and P_C= 0.086%
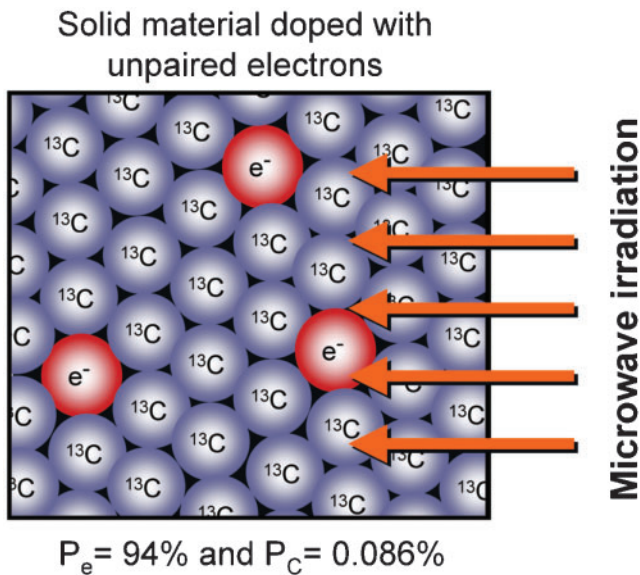
Figure 2. During the dynamic nuclear polarization process, polarization is transferred from the electrons of the doping material to the ^{13}C nuclei by means of microwave irradiation.

reaction involving parahydrogen; a state where the hydrogen nuclei are oriented such that their magnetic moments cancel (Figure 3). Bowers and Weitekamp initially predicted and verified that the PHIP effect arises in molecules catalytically hydrogenated with parahydrogen [13, 14]. A prerequisite is that the hydrogenation mechanism operates by transfer of the hydrogen molecule as a unit onto the substrate (Figure 4a). By means of a diabatic field cycling scheme, the non-equilibrium spin order of the parahydrogen molecule is then converted to nuclear polarization of the ^{13}C nucleus in the substrate (Figure 4b) [15].

Optical pumping methods

In 1960, Bouchiat et al [16] showed that angular momentum could be transferred from the electron spins of optically pumped Rb atoms [17] to the nuclear spins of ^{3}He by spin-exchange collisions. The method could be extended to efficiently polarize ^{129}Xe as well [18]. In a magnetic field, the electronic transition $S_{1/2}$–$P_{1/2}$ of the Rb atoms can be driven by circularly polarized laser light (795 nm), to selectively pump the ground-state Rb electrons entirely to the $+\frac{1}{2}$ (or $-\frac{1}{2}$) state. The electronic
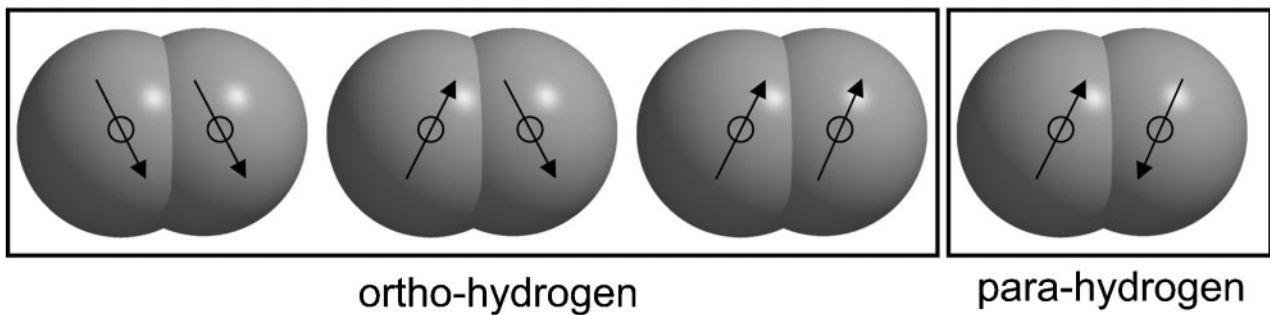
Figure 3. The four possible orientations of the nuclear spin in the hydrogen molecule.
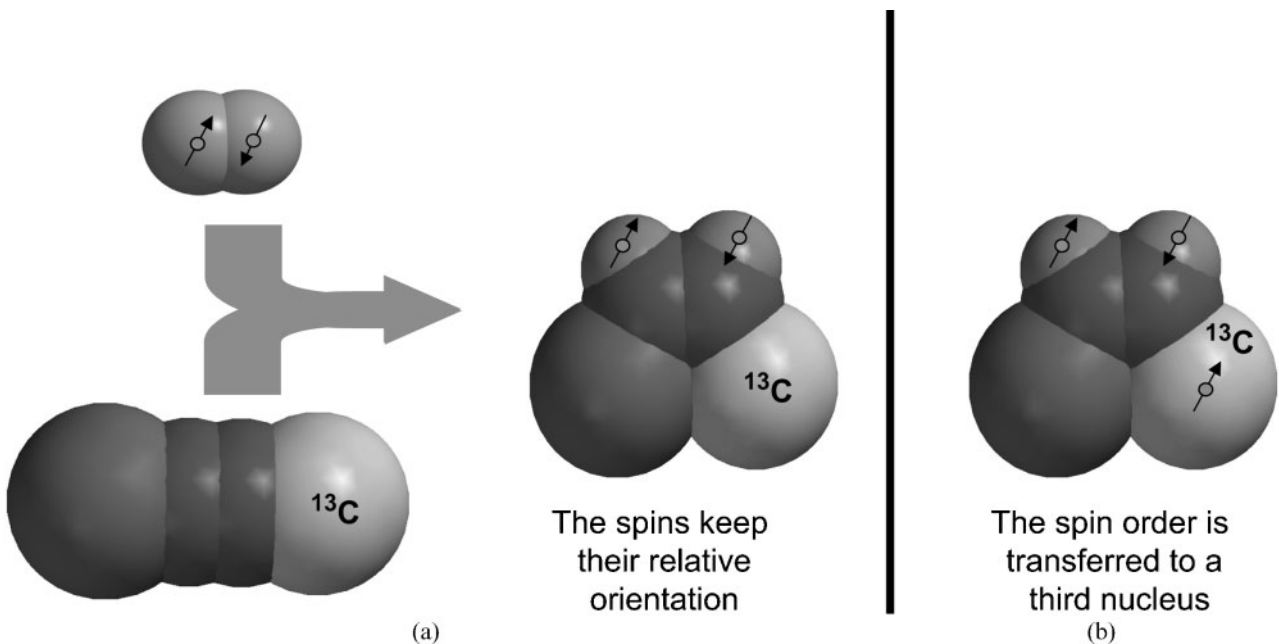
Figure 4. (a) A substrate molecule containing ^{13}C is hydrogenated with parahydrogen. (b) The spin order of the parahydrogen molecule is converted to nuclear polarization of the ^{13}C nucleus, via a diabatic field cycling scheme.

polarization of the optically pumped Rb atoms is transferred to the nuclei of the noble gas atoms via formation of loosely bound van der Waals molecules or via binary collisions. The process creates a non-equilibrium polarization of the noble gas nuclei.

Hyperpolarization of ^{3}He can also be achieved by the method of metastability exchange, first reported in 1958 [19]. In a low-pressure ^{3}He gas (about 1–2 mbar), $^3S_1$ metastable atoms are formed by a weak electrical discharge. By using circularly polarized light, transitions $^3S_1 \rightarrow ^3P_0$ (1083.0 nm) are induced. Due to strong hyperfine coupling, the nuclei of metastable atoms become polarized. When a polarized metastable atom collides with an unpolarized ground-state atom, a high probability for exchange of metastability exists: the metastable and the ground-state atom exchange their electron configurations, while the nuclear polarization remains unaffected. Thus, the collision yields a polarized ground-state atom and a non-polarized metastable atom. The latter can once more undergo the optical pumping process [20–22]. A classic review of optical pumping methods has been given by Happer [23].

Although the theory of hyperpolarizing noble gases by optical pumping was known in the early 1960s, large-scale production has only recently been possible, owing to the development of high-power lasers [24, 25]. An overview of the methods for hyperpolarization of noble gases was recently published by Goodson [26].

Medical applications of hyperpolarized nuclei: a brief overview

Lung imaging

With the advent of the hyperpolarized noble gases ^{3}He and ^{129}Xe, a natural tool was provided for imaging of the lung, which is a difficult area for ^{1}H MRI because of the low density of protons in the lung parenchyma and the strong susceptibility gradients at the gas–tissue interface [27, 28]. In 1994, the first MR images using hyperpolarized gas were demonstrated, showing excised mouse lungs filled with ^{129}Xe [5]. The first ^{3}He images depicting the lungs of a dead guinea pig were presented in 1995 [6]. These initial works were followed by the first human images using ^{3}He [29–31] and ^{129}Xe [32, 33]. For a review of the historical background of hyperpolarized lung imaging see Albert and Balamore [9].

The diagnostic potential of hyperpolarized gas imaging was first demonstrated in studies revealing various ventilation defects in patients, where non-ventilated regions were depicted as signal voids [34]. Rapid dynamic imaging has also demonstrated the potential to detect abnormal breathing patterns caused by lung disease [35–37] and to quantify ventilation [38]. An example of a three-dimensional (3D) ventilation quantification is shown in Figure 5. Owing to the large diffusion coefficient of gases (especially ^{3}He), the image intensity will decrease in regions with elevated mobility of the gas [39, 40]. By measuring the apparent diffusion coefficient (ADC), it is thus possible to gain information of pathological lung structure, *e.g.* in emphysematous lungs [41]. From measurements of the T_1 relaxation time, it has further been possible to calculate the regional oxygen partial pressure pO_2 in the lungs based on the depolarizing effect of O_2 [42–44]. The ventilation–perfusion ratio (V_A / Q) is highly relevant for the diagnosis

of abnormal lung function [45]. By combining ^{3}He ventilation imaging with ^{1}H perfusion imaging, initial attempts have been made to assess the V_A / Q parameter in animals [46–48] and in humans [49, 50].

Multichannel receiver systems on modern MRI instruments allow detection of several nuclei simultaneously. Simultaneous acquisition of ^{3}He and ^{1}H images is therefore possible, and — even more fascinating — ^{13}C images. By injecting a hyperpolarized ^{13}C-labelled substance intravenously, we have obtained images of the pulmonary arterial circulation (Figure 6). Images of hyperpolarized ^{3}He and ^{13}C can be acquired in <1 s, and it may be possible to study regional ventilation and perfusion in "real-time" if a ^{13}C substance is injected simultaneously with administration of ^{3}He. The location and functional importance of pulmonary emboli may thus be quantified.

Organs other than the lungs

Owing to its solubility in blood and tissues, inhaled ^{129}Xe is distributed throughout the body, and can thus be used for applications other than lung imaging [32]. The resonance frequency of ^{129}Xe dissolved in liquids is ~200 ppm higher than in the gas phase [51], and varies over a ~20 ppm range in tissues *in vivo* [52, 53]. Because the resonance frequency of ^{129}Xe is sensitive to its local environment, numerous experiments involving spectroscopy or chemical shift imaging (CSI) have been presented, *e.g.* CSI of the chest and the brain [54, 55], spectroscopy of tumours [56] and probing of the pO_2 in blood [57]. Using the large frequency shift between the gas phase and the dissolved phase ^{129}Xe, methods have been proposed to monitor the dynamics of ^{129}Xe when transported from the alveoli to the pulmonary blood [58–60], from which information about the diffusing capacity of the lung can be obtained.

The spectral information obtained from CSI is a strength of MRI compared with other modalities, since it informs about the molecular structure and the environment of the molecule. The chemical shift of ^{129}Xe is based only on the different environments, whereas for ^{13}C-labelled substances, it is mainly the molecular structure that determines the chemical shift. CSI has been used to image the localization of metabolites within the brain of ^{13}C labelled substances (*e.g.* glucose, alanine etc.) [61]. Without hyperpolarization, very long scan times have been needed to generate such images. To image the metabolic processes in a clinically relevant time frame (seconds), hyperpolarization is needed.

Vascular imaging with hyperpolarized ^{13}C

Hyperpolarized ^{13}C has only recently been available at polarization levels sufficient for MRI [8, 15, 62, 63]. At present, a polarization of 10–30% can be obtained, and the long relaxation times (T_1 and T_2 up to ~60 s and 5 s, respectively) makes "real-time" vascular imaging with ^{13}C molecules a new tool to examine pathological conditions. The feasibility of hyperpolarized ^{13}C for MR angiography has recently been investigated [64].

Molecular imaging applications

With the possibility to polarize ^{13}C-labelled molecules to >20%, MRI may emerge beyond anatomical (*e.g.* angiography) and functional (*e.g.* perfusion and diffusion)
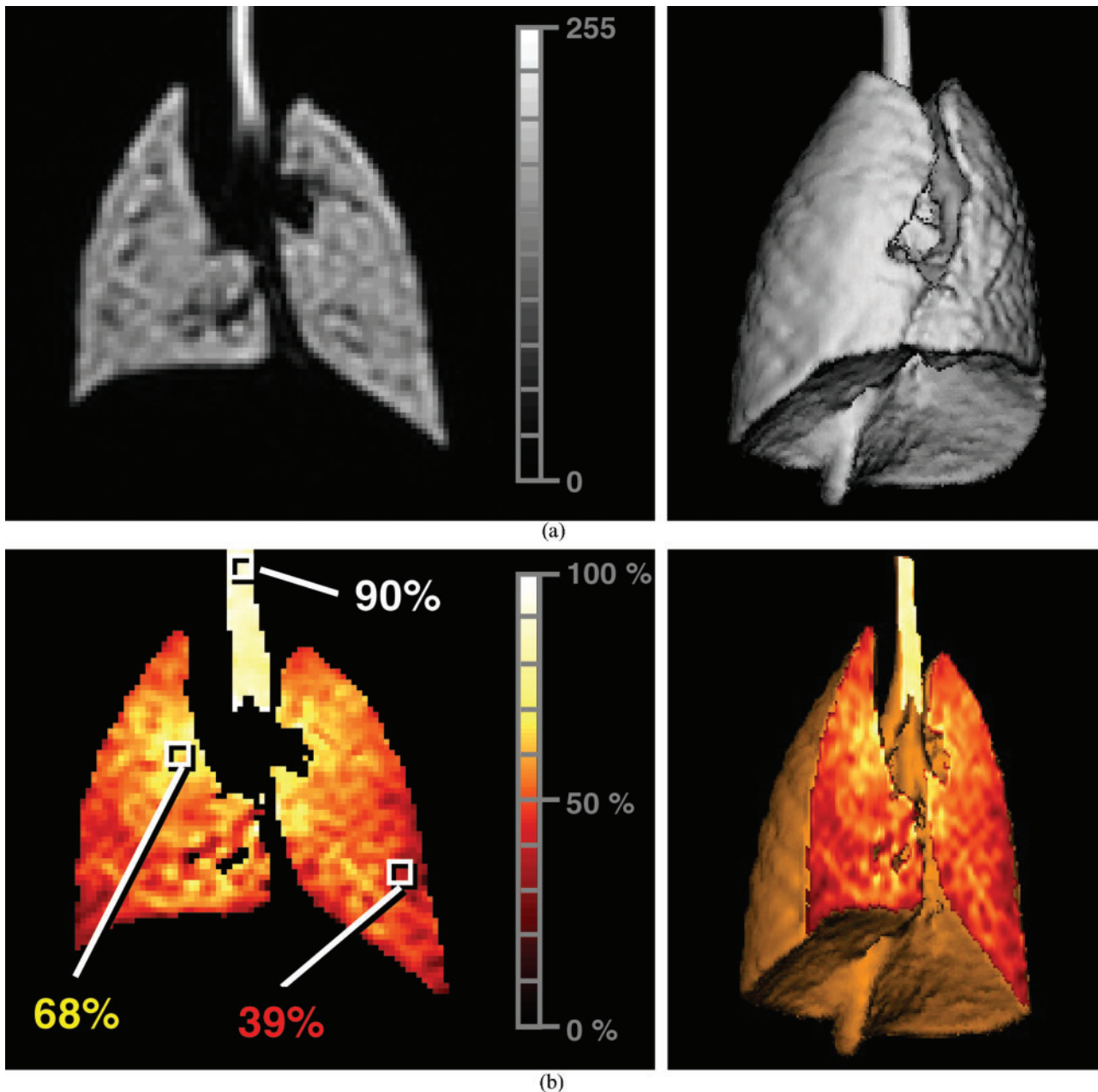
Figure 5. (a) Three-dimensional ^{3}He image of a rat lung (central slice and surface rendering). (b) The corresponding quantitative ventilation map calculated according to the method described by Deninger et al [38].

visualization. Since hyperpolarized ^{13}C MRI directly informs about the molecules, to which the hyperpolarized atoms are attached, investigation of tissue and cell viability (direct molecular imaging) may be feasible.

In the following, we present a study in which the PHIP method was employed to polarize a ^{13}C-labelled, water-soluble molecule to ~30%, followed by *in vivo* imaging of the distribution of the ^{13}C molecule, after intravenous injection in rabbits.

Methods and materials

### The molecular imaging agent

The ^{13}C-labelled molecule (2-hydroxyethylacrylate, molecular weight ~120 g mol^{-1}) was polarized using an automated version of the parahydrogen process described elsewhere [15]. A polarization level of ~30% was achieved and a volume of 2.5 ml 0.5 M solution was produced for each injection. The polarization level had been determined from a series of calibration experiments on a 7 T spectrometer (Varian, Palo Alto, CA), by comparing the integral of a ^{13}C spectrum acquired from a hyperpolarized sample, and a second spectrum acquired from the same sample after the polarization had decayed to thermal equilibrium.

Animals

Four rabbits (male, Swedish loop, 2.1–4.0 kg) were anaesthetized intramuscularly with butorphanol (Torbugesic®; Fort Dodge Animal Health, Fort Dodge,
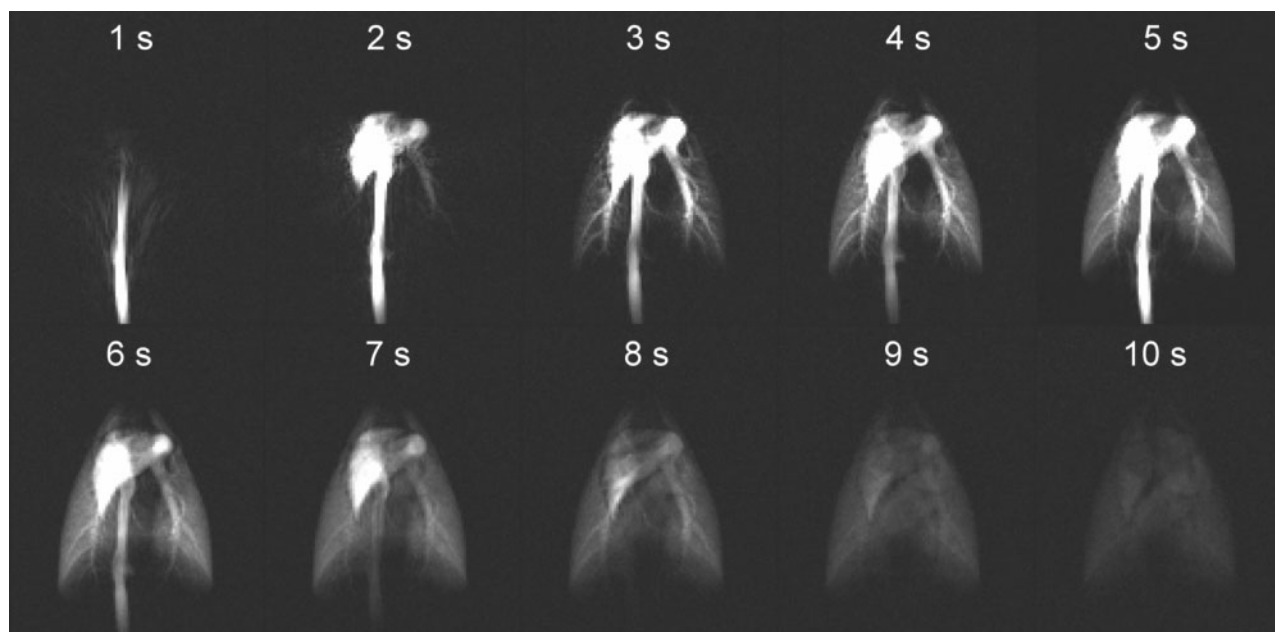
Figure 6. A series of trueFISP ^{13}C images, showing the lungs of a pig after injection of a hyperpolarized ^{13}C imaging agent. The imaging sequence was repeated with 1 s intervals.

USA), xylazine (Rompun® vet.; Bayer AG, Leverkusen, Germany) and ketamine (Ketalar®; Pfizer Inc., New York, NY). The imaging agent was administrated through a venflon catheter placed in an ear vein. During the imaging procedure, anaesthesia was titrated as necessary. All animals were sacrificed after completion of imaging. The study was approved by the local ethics committee (Malmö/Lunds djurförsöksetiska nämnd; appl. no. M92–01).

MRI equipment

All MRI measurements were performed in a 1.5 T whole-body scanner (Magnetom Sonata; Siemens Medical Solutions, Erlangen, Germany). The scanner needed no extra modification, except for the coil for ^{13}C imaging. A custom built, dual tuned $^{1}H/^{13}C$ transmit/receive coil (Rapid Biomedical GmbH., Würzburg, Germany) was used. The ^{13}C part of the coil was built as a birdcage (Ø=170 mm, length=170 mm), and consisted of two elements in quadrature. Tuning and matching of the coil was performed individually for each rabbit.

MRI examinations

Three out of the four rabbits (in the following referred to as Rabbit 1–3) were used for ^{13}C imaging to evaluate the hyperpolarized imaging agent. The fourth rabbit (referred to as Rabbit 4) was used to acquire reference proton images, and was injected with the conventional Gd-based contrast agent OMNISCAN™ (Amersham Health, Oslo, Norway). All animals were positioned supine and proton localizer images were acquired in order to fit the heart/lung and the kidneys in the expected field of view (FOV). During the ^{13}C imaging procedure (Rabbit 1–3), the scanner frequency was set to the ^{13}C resonance using a measured relationship between the ^{1}H resonance frequency and the ^{13}C frequency of the imaging agent.

All imaging was performed using a trueFISP [65] sequence with a high flip angle (α=160°), which has been found superior for MRI of hyperpolarized ^{13}C substances [64]. The trueFISP sequence was preceded by a $\alpha/2$ preparation pulse, and a centric encoding scheme was used for the phase encoding gradient. The sequence is shown schematically in Figure 7. The imaging volume consisted of coronal slices with a thickness larger than the animal (projection imaging). The in-plane spatial resolution was increased in Rabbit 3 (1.0×1.0 mm^2 pixel size, compared with 2.5×2.5 mm^2 in Rabbits 1–2). The echo time (TE) and repetition time (TR) were the shortest possible for the selected in-plane spatial resolution (TR/TE=4.9/2.5 ms for Rabbits 1–2, TR/TE=8.9/4.5 ms for Rabbit 3). Due to the low gyromagnetic ratio of the ^{13}C nucleus, the gradient performance was the limiting factor for achieving short TR. In all ^{13}C experiments, the volume and concentration of the injected molecular imaging agent was 2.5 ml and 0.5 M, respectively. The scanning was started 2 s, 4 s and 6 s after the end of the injection.

The Gd contrast agent injected in Rabbit 4 was diluted 1:5 to obtain an injection volume equal to the ^{13}C injections in Rabbits 1–3. A dynamic 3D ^{1}H study with a temporal resolution of 0.86 s was performed. The spatial resolution was 1.5×1.5 mm^2. The image information in the partitions covering the animal was added to a single slab per time point, resulting in one projection image for each time point.

To quantitatively evaluate the images, a region of interest (ROI) was located over specific regions or organs. Signal-to-noise ratios (SNRs) were calculated from the mean signal in a ROI divided by the mean noise value in a ROI outside the animal and free from imaging artefacts.

Results

During the experiments, a new syringe with the imaging agent could be produced with 2 min intervals. With the

Image generation
Phase-encoding loop
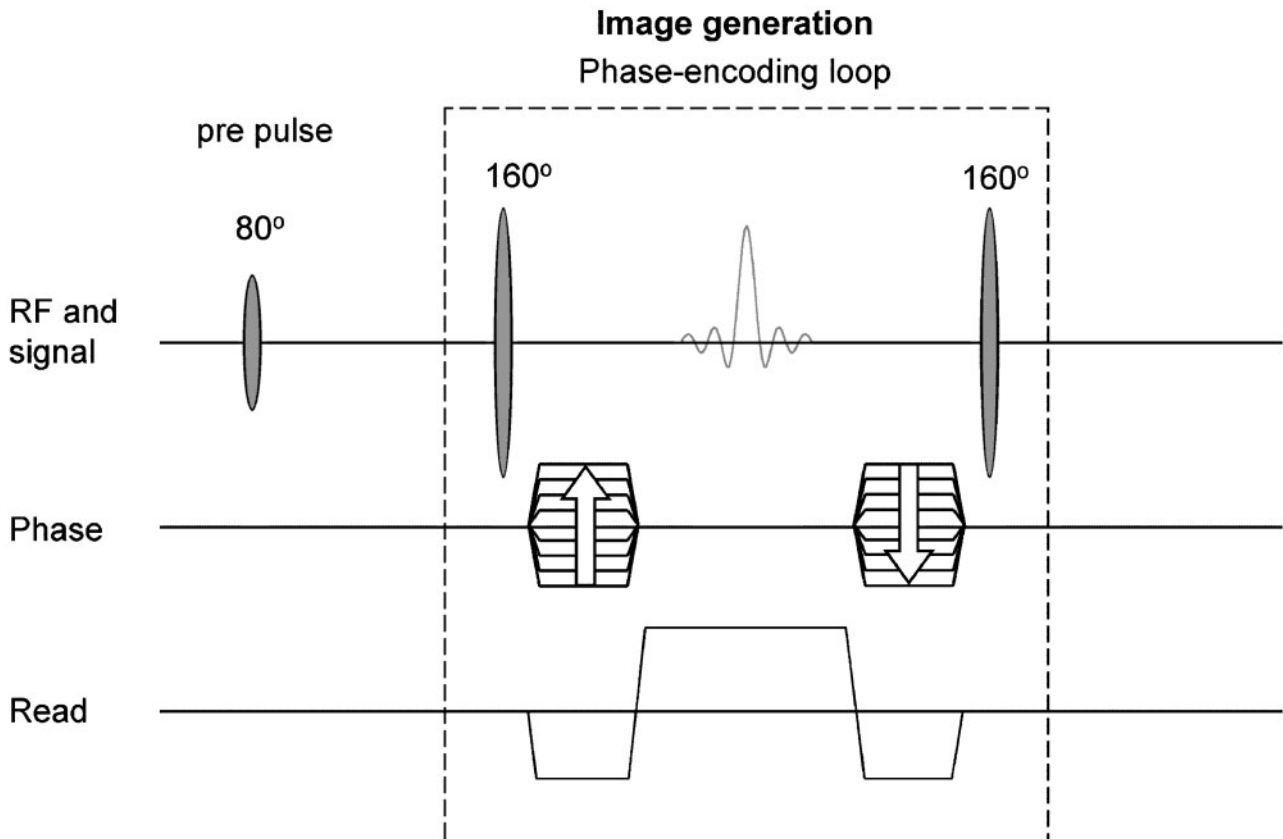
Figure 7. Schematic drawing of the trueFISP sequence.

polarization level of ~30%, it was possible to perform ^{13}C imaging of live rabbits with a spatial resolution of 1×1 mm^2. The signal strength from the molecular imaging agent was sufficient to trace the distribution of the agent into several organs.

The distribution of the ^{13}C imaging agent at different time points is depicted in Figure 8. Two seconds after the injection, the imaging agent is mainly located in the heart and the lungs, but there is also signal from the kidneys (Figure 8a). There is a considerable amount of image artefacts, especially ringing artefacts emanating from the aorta and the heart. 4 s after the injection, the signal in the lungs and the aorta has decreased (Figure 8b). The signal from the kidneys has increased, and structures within the kidney parenchyma are distinguishable. A definition of the stomach wall is now clearly visible, contrary to the Gd-enhanced ^{1}H image, which did not show this anatomic structure. 6 s after the injection, the intestines are visible, in addition to the stomach walls (Figure 8c). This again differs from what could be seen with the Gd-based contrast agent.

Discussion

In this study, the first MR images of live animals injected with a ^{13}C substance, hyperpolarized with the PHIP method, are presented. With the present polarization levels (~30%), *in vivo* images with SNR between 20 and 60 in various organs were achieved after injection of 2.5 ml 0.5 M molecular imaging agent in rabbits. Images could be acquired with a spatial resolution of 1.0×1.0 mm^2. Initially, the distribution of the ^{13}C substance was similar

to that of the conventional Gd-based contrast agent, a finding supported by a quantitative ROI evaluation of the SNR in the heart, lung, kidney and aorta, but already 4 s after the injection other structures, such as the stomach wall, was seen in the ^{13}C images. This could not be observed in the corresponding Gd-enhanced ^{1}H images.

During the first few seconds after the injection, most of the ^{13}C imaging agent is still present in the blood and the highest vascularized organs, *i.e.* the heart, the lungs and the kidneys. The ^{13}C imaging agent is a small molecule (molecular weight ~120 g mol^{-1}) and leaks out rapidly into the extravascular space; already after a few seconds, there is a significant uptake in soft tissues.

It can be observed that the ^{13}C images have lower signal than expected in the aorta and other large vessels. The low signal in these vessels may be explained by flow losses, since the echo times were rather long, despite the shortest possible settings being used. Because the gyromagnetic ratio for ^{13}C is four times lower than for ^{1}H, longer echo times are compelled since the gradient strength is finite (40 mT m^{-1}). This explanation is further supported by the fact that large vessels were clearly depicted when a hyperpolarized ^{13}C substance was imaged with echo times <2 ms on a different type of MR scanner with 200 mT m^{-1} gradients [64].

Since the natural abundance of ^{13}C is far below the detection limit of a MRI scanner, the background signal in ^{13}C MRI is reduced to the noise produced by the imaged object and the detection system. This suggests that the contrast-to-noise ratio will be high and, at least initially, equals the SNR. Accordingly, thick imaging slices, or even projection techniques, may be used to visualize the distribution of the molecular imaging agent.
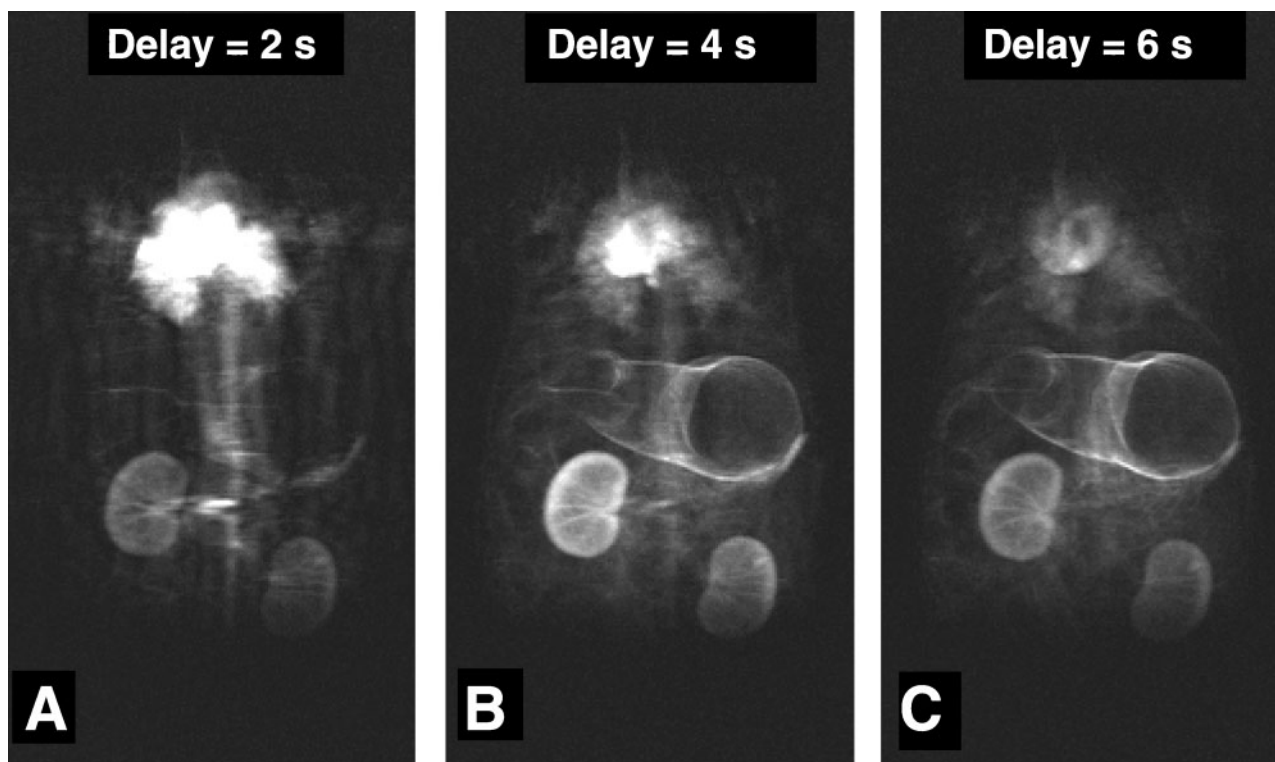
Figure 8. Images depicting the distribution of the injected hyperpolarized ^{13}C imaging agent at different times after the injection. The delay between injection and imaging is indicated at the top of each image.

Hyperpolarized MRI differs from conventional MRI, in the sense that any magnetization used up by the imaging process cannot be recovered. The obvious drawback is that the imaging protocol gets restricted [66, 67], and the time window for imaging is limited. Typically, several images with high temporal resolution are needed to study the distribution of a contrast agent. In this study, only one image was acquired for each injection. A technique to preserve the magnetization between subsequent images has been presented [64], but was not available on the scanner used in this study.

The introduction of an injectable, hyperpolarized ^{13}C substance opens a new field of MRI. With the coil and the receiver system of the scanner tuned to the resonance frequency of the hyperpolarized nucleus, only signals from the injected substance will be detected. The signal strength is a linear function of the concentration and the polarization level of the nucleus in question. This is not the case for a conventional contrast agent (*e.g.* Gd-chelates and other paramagnetic molecules/particles) that operates by altering the relaxation times of water protons in surrounding tissues [68–70]. When irradiated with a radiofrequency wave, the injected ^{13}C nuclei emits a radiofrequency signal, contrary to the tracer substance used in PET or SPECT imaging, which emits γ-rays. More information can be obtained from an NMR-active nucleus, since its resonance frequency is a function of its chemical and physiological environment (*e.g.* chemical shielding, viscosity and mobility). Thereby, it is possible to separate the signals from ^{13}C nuclei within different molecules. This feature is exploited in the field of analytical NMR spectroscopy and *in vivo* MR spectroscopy. While PET and SPECT are only capable of mapping the distribution of the nuclei, regardless if they are still contained within the injected molecules or not, NMR is capable of distinguishing signals from the tracer nuclei (*e.g.* ^{13}C) present in different molecules. This specificity on a molecular level is the basis for the clinical use of MR spectroscopy [71–73]. Due to SNR limitations, this has been restricted to protons, ^{19}F and ^{31}P, and to the use of large image voxels (~ 1 cm^3). The hyperpolarization procedure used in the present work overcomes these restrictions, but still retains the specificity of the NMR technique, and thus makes it possible to perform direct molecular imaging. Consequently, distribution patterns may be mapped by injection and imaging of several hyperpolarized ^{13}C molecules simultaneously, delivering valuable information about membrane structure and permeability.

Conclusion

We have demonstrated that it is feasible to image hyperpolarized ^{13}C-labelled molecules with MRI. The technique is in its infancy, and improvements with respect to polarization and imaging techniques seem possible. MRI as an image modality offers, in connection with a ^{13}C-labelled image agent the possibility of obtaining information about molecular behaviour *in vivo*. The choice of substance to be hyperpolarized will influence the medical information obtained.

Acknowledgments

References

1. Edelstein WA, Glover GH, Hardy CJ, Redington RW. The intrinsic signal-to-noise ratio in NMR imaging. Magn Reson Med 1986;3:604–18.

2. Campeau NG, Huston J 3rd, Bernstein MA, Lin C, Gibbs GF. Magnetic resonance angiography at 3.0 Tesla: initial clinical experience. Top Magn Reson Imaging 2001; 12:183–204.

3. Overhauser AW. Polarization of nuclei in metals. Phys Rev 1953;92:411–5.

4. Golman K, Petersson JS, Ardenkjaer-Larsen JH, Leunbach I, Wistrand LG, Ehnholm G, et al. Dynamic in vivo oxymetry using overhauser enhanced MR imaging. J Magn Reson Imaging 2000;12:929–38.

5. Albert MS, Cates GD, Driehuys B, Happer W, Saam B, Springer CS Jr, et al. Biological magnetic resonance imaging using laser-polarized ^{129}Xe. Nature 1994;370:199–201.

6. Middleton H, Black RD, Saam B, Cates GD, Cofer GP, Guenther R, et al. MR imaging with hyperpolarized ^{3}He gas. Magn Reson Med 1995;33:271–5.

7. Golman K, Axelsson O, Johannesson H, Mansson S, Olofsson C, Petersson JS. Parahydrogen-induced polarization in imaging: subsecond ^{13}C angiography. Magn Reson Med 2001;46:1–5.

8. Ardenkjaer-Larsen JH, Fridlund B, Gram A, Hansson G, Hansson L, Lerche MH, et al. Increase in signal-to-noise ratio of >10,000 times in liquid-state NMR. Proc Natl Acad Sci USA 2003;100:10158–63.

9. Albert MS, Balamore D. Development of hyperpolarized noble gas MRI. Nucl Instrum Methods Phys Res A 1998;402:441–53.

10. Merbach A, Tóth É, editors. The chemistry of contrast agents in medical magnetic resonance imaging. Chichester: John Wiley & Sons, 2001.

11. Frossati G. Polarization of ^{3}He, D_2 (and possibly ^{129}Xe) using cryogenic techniques. Nucl Instrum Meth A 1998;402: 479–83.

12. Abragam A, Goldman M. Principles of dynamic nuclear polarisation. Rep Prog Phys 1978;41:395–467.

13. Bowers CR, Weitekamp DP. Transformation of symmetrization order to nuclear-spin magnetization by chemical reaction and nuclear magnetic resonance. Phys Rev Lett 1986;57: 2645–8.

14. Bowers CR, Weitekamp DP. Parahydrogen and synthesis allow dramatically enhanced nuclear alignment. J Am Chem Soc 1987;109:5541–2.

15. Jóhannesson H, Axelsson O, Karlsson M. Transfer of parahydrogen spin order into polarization by diabatic field cycling. C R Physique 2004;5:315–24.

16. Bouchiat MA, Carver TR, Varnum CM. Nuclear polarization in He^{3} gas induced by optical pumping and dipolar exchange. Phys Rev Lett 1960;5:373–5.

17. Kastler A. Quelques suggestions concernant la production optique et la detection optique d'une inégalité de population des niveaux de quantification spatiale des atomes: application à l'expérience de Stern et Gerlach et à la résonance magnétique. J Phys Rad 1950;11:255–65.

18. Grover BC. Noble-gas NMR detection through noble-gas-rubidium hyperfine contact interaction. Phys Rev Lett 1978;40:391–2.

19. Franken PA, Colegrove FD. Alignment of metastable helium atoms by unpolarized resonance radiation. Phys Rev Lett 1958;1:316–8.

20. Colegrove FD, Franken PA. Optical pumping of helium in the $^{3}S_1$ metastable state. Phys Rev 1960;119:680–90.

21. Colegrove FD, Schearer LD, Walters GK. Polarization of He^{3} gas by optical pumping. Phys Rev 1963;132:2561–72.

22. Gamblin RL, Carver TR. Polarization and relaxation processes in He^{3} gas. Phys Rev 1965;138:A946–A60.

23. Happer W. Optical pumping. Rev Mod Phys 1972;44: 169–249.

24. Daniels JM, Shearer LD, Leduc M, Nacher PJ. Polarizing ^{3}He nuclei with neodymium La$_{1-x}$Nd$_x$MgAl$_{11}$O$_{19}$ lasers. J Opt Soc Am 1987;B4:1133–5.

25. Driehuys B, Cates GD, Miron E, Sauer K, Walter DK, Happer W. High-volume production of laser-polarized ^{129}Xe. Appl Phys Lett 1996;69:1668–70.

26. Goodson BM. Nuclear magnetic resonance of laser-polarized noble gases in molecules, materials, and organisms. J Magn Reson 2002;155:157–216.

27. Bergin CJ, Glover GH, Pauly JM. Lung parenchyma: magnetic susceptibility in MR imaging. Radiology 1991; 180:845–8.

28. Bergin CJ, Glover GM, Pauly J. Magnetic resonance imaging of lung parenchyma. J Thorac Imaging 1993;8:12–7.

29. MacFall JR, Charles HC, Black RD, Middleton H, Swartz JC, Saam B, et al. Human lung air spaces: potential for MR imaging with hyperpolarized ^{3}He. Radiology 1996;200:553–8.

30. Bachert P, Schad LR, Bock M, Knopp MV, Ebert M, Grossmann T, et al. Nuclear magnetic resonance imaging of airways in humans with use of hyperpolarized ^{3}He. Magn Reson Med 1996;36:192–6.

31. Ebert M, Grossmann T, Heil W, Otten WE, Surkau R, Leduc M, et al. Nuclear magnetic resonance imaging with hyperpolarised ^{3}He. Lancet 1996;347:1297–9.

32. Mugler JP 3rd, Driehuys B, Brookeman JR, Cates GD, Berr SS, Bryant RG, et al. MR imaging and spectroscopy using hyperpolarized ^{129}Xe gas: preliminary human results. Magn Reson Med 1997;37:809–15.

33. Albert MS, Tseng CH, Williamson D, Oteiza ER, Walsworth RL, Kraft B, et al. Hyperpolarized ^{129}Xe MR imaging of the oral cavity. J Magn Reson B 1996;111:204–7.

34. Kauczor HU, Hofmann D, Kreitner KF, Nilgens H, Surkau R, Heil W, et al. Normal and abnormal pulmonary ventilation: visualization at hyperpolarized ^{3}He MR imaging. Radiology 1996;201:564–8.

35. Johnson GA, Cates G, Chen XJ, Cofer GP, Driehuys B, Happer W, et al. Dynamics of magnetization in hyperpolarized gas MRI of the lung. Magn Reson Med 1997;38:66–71.

36. Gierada DS, Saam B, Yablonskiy D, Cooper JD, Lefrak SS, Conradi MS. Dynamic echo planar MR imaging of lung ventilation with hyperpolarized ^{3}He in normal subjects and patients with severe emphysema. NMR Biomed 2000;13:176–81.

37. Salerno M, Altes TA, Brookeman JR, de Lange EE, Mugler JP 3rd. Dynamic spiral MRI of pulmonary gas flow using hyperpolarized ^{3}He: preliminary studies in healthy and diseased lungs. Magn Reson Med 2001;46:667–77.

38. Deninger AJ, Mansson S, Petersson JS, Pettersson G, Magnusson P, Svensson J, et al. Quantitative measurement of regional lung ventilation using ^{3}He MRI. Magn Reson Med 2002;48:223–32.

39. Chen XJ, Möller HE, Chawla MS, Cofer GP, Driehuys B, Hedlund LW, et al. Spatially resolved measurements of hyperpolarized gas properties in the lung in vivo. Part I: diffusion coefficient. Magn Reson Med 1999;42:721–8.

40. Yablonskiy DA, Sukstanskii AL, Leawoods JC, Gierada DS, Bretthorst GL, Lefrak SS, et al. Quantitative in vivo assessment of lung microstructure at the alveolar level with hyperpolarized ^{3}He diffusion MRI. Proc Natl Acad Sci USA 2002;99:3111–6.

41. Saam BT, Yablonskiy DA, Kodibagkar VD, Leawoods JC, Gierada DS, Cooper JD, et al. MR imaging of diffusion of ^{3}He gas in healthy and diseased lungs. Magn Reson Med 2000;44:174–9.

42. Deninger AJ, Eberle B, Bermuth J, Escat B, Markstaller K, Schmiedeskamp J, et al. Assessment of a single-acquisition imaging sequence for oxygen-sensitive ^{3}He-MRI. Magn Reson Med 2002;47:105–14.

43. Deninger AJ, Eberle B, Ebert M, Grossmann T, Heil W, Kauczor H, et al. Quantification of regional intrapulmonary oxygen partial pressure evolution during apnea by ^{3}He MRI. J Magn Reson 1999;141:207–16.

44. Möller HE, Hedlund LW, Chen XJ, Carey MR, Chawla MS, Wheeler CT, et al. Measurements of hyperpolarized gas properties in the lung. Part III: ^{3}He T_1. Magn Reson Med 2001;45:421–30.

45. Guyton AC. Textbook of medical physiology. Philadelphia, PA: W. B. Saunders, 1986.

46. Cremillieux Y, Berthezene Y, Humblot H, Viallon M, Canet E, Bourgeois M, et al. A combined ^{1}H perfusion/^{3}He ventilation NMR study in rat lungs. Magn Reson Med 1999;41:645–8.

47. Rizi RR, Saha PK, Wang B, Ferrante MA, Lipson D, Baumgardner J, et al. Coregistration of acquired MR ventilation and perfusion images—validation in a porcine model. Magn Reson Med 2003;49:13–8.

48. Jalali A, Ishii M, Edvinsson JM, Guan L, Itkin M, Lipson DA, et al. Detection of simulated pulmonary embolism in a porcine model using hyperpolarized ^{3}He MRI. Magn Reson Med 2004;51:291–8.

49. Lipson DA, Roberts DA, Hansen-Flaschen J, Gentile TR, Jones G, Thompson A, et al. Pulmonary ventilation and perfusion scanning using hyperpolarized ^{3}He MRI and arterial spin tagging in healthy normal subjects and in pulmonary embolism and orthotopic lung transplant patients. Magn Reson Med 2002;47:1073–6.

50. Rizi RR, Lipson DA, Dimitrov IE, Ishii M, Roberts DA. Operating characteristics of hyperpolarized ^{3}He and arterial spin tagging in MR imaging of ventilation and perfusion in healthy subjects. Acad Radiol 2003;10:502–8.

51. Miller KW, Reo NV, Schoot Uiterkamp AJ, Stengle DP, Stengle TR, Williamson KL. Xenon NMR: chemical shifts of a general anesthetic in common solvents, proteins, and membranes. Proc Natl Acad Sci USA 1981;78:4946–9.

52. Wagshul ME, Button TM, Li HF, Liang Z, Springer CS, Zhong K, et al. In vivo MR imaging and spectroscopy using hyperpolarized ^{129}Xe. Magn Reson Med 1996;36:183–91.

53. Sakai K, Bilek AM, Oteiza E, Walsworth RL, Balamore D, Jolesz FA, et al. Temporal dynamics of hyperpolarized ^{129}Xe resonances in living rats. J Magn Reson B 1996;111:300–4.

54. Swanson SD, Rosen MS, Agranoff BW, Coulter KP, Welsh RC, Chupp TE. Brain MRI with laser-polarized ^{129}Xe. Magn Reson Med 1997;38:695–8.

55. Swanson SD, Rosen MS, Coulter KP, Welsh RC, Chupp TE. Distribution and dynamics of laser-polarized ^{129}Xe magnetization in vivo. Magn Reson Med 1999;42:1137–45.

56. Wolber J, McIntyre DJ, Rodrigues LM, Carnochan P, Griffiths JR, Leach MO, et al. In vivo hyperpolarized ^{129}Xe NMR spectroscopy in tumors. Magn Reson Med 2001;46:586–91.

57. Wolber J, Cherubini A, Leach MO, Bifone A. Hyperpolarized ^{129}Xe NMR as a probe for blood oxygenation. Magn Reson Med 2000;43:491–6.

58. Mansson S, Wolber J, Driehuys B, Wollmer P, Golman K. Characterization of diffusing capacity and perfusion of the rat lung in a lipopolysaccaride disease model using hyperpolarized ^{129}Xe. Magn Reson Med 2003;50:1170–9.

59. Ruppert K, Brookeman JR, Hagspiel KD, Driehuys B, Mugler JP 3rd. NMR of hyperpolarized ^{129}Xe in the canine chest: spectral dynamics during a breath-hold. NMR Biomed 2000;13:220–8.

60. Ruppert K, Brookeman JR, Hagspiel KD, Mugler JP 3rd. Probing lung physiology with xenon polarization transfer contrast (XTC). Magn Reson Med 2000;44:349–57.

61. Sonnewald U, Gribbestad IS, Westergaard N, Nilsen G, Unsgard G, Schousboe A, et al. Nuclear magnetic resonance spectroscopy: biochemical evaluation of brain function in vivo and in vitro. Neurotoxicology 1994;15:579–90.

62. Golman K, Ardenkjaer-Larsen JH, Svensson J, Axelsson O, Hansson G, Hansson L, et al. ^{13}C-angiography. Acad Radiol 2002;9:Suppl 2, S507–S10.

63. Golman K, Ardenkjaer-Larsen JH, Petersson JS, Mansson S, Leunbach I. Molecular imaging with endogenous substances. Proc Natl Acad Sci USA 2003;100:10435–9.

64. Svensson J, Mansson S, Johansson E, Petersson JS, Olsson LE. Hyperpolarized ^{13}C MR angiography using trueFISP. Magn Reson Med 2003;50:256–62.

65. Oppelt A, Graumann R, Barfuss H, Fischer H, Hartl W, Schajor W. FISP: Eine neue schnelle Pulssequenz für die Kernspintomographie. Electromedica 1986;54:15–8.

66. Zhao L, Albert MS. Biomedical imaging using hyperpolarized noble gas MRI: pulse sequence considerations. Nucl Instrum Methods Phys Res A 1998;402:454–60.

67. Markstaller K, Eberle B, Schreiber WG, Weiler N, Thelen M, Kauczor HU. Flip angle considerations in (3)helium-MRI. NMR Biomed 2000;13:190–3.

68. Nishimura DG, Macovski A, Pauly JM. Magnetic resonance angiography. IEEE Trans Med Imaging 1986;5:140–51.

69. Maki JH, Chenevert TL, Prince MR. Three-dimensional contrast-enhanced MR angiography. Top Magn Reson Imaging 1996;8:322–44.

70. Prince MR, Yucel EK, Kaufman JA, Harrison DC, Geller SC. Dynamic gadolinium-enhanced three-dimensional abdominal MR arteriography. J Magn Reson Imaging 1993;3:877–81.

71. Ross B, Michaelis T. Clinical applications of magnetic resonance spectroscopy. Magn Reson Q 1994;10:191–247.

72. Cousins JP. Clinical MR spectroscopy: fundamentals, current applications, and future potential. AJR Am J Roentgenol 1995;164:1337–47.

73. Henriksen O. MR spectroscopy in clinical research. Acta Radiol 1994;35:96–116.